

The globular cluster system of NGC 1316*

IV. Nature of the star cluster complex SH2

T. Richtler¹, B. Husemann^{6,2}, M. Hilker², T. H. Puzia³, F. Bresolin⁴, and M. Gómez⁵

¹ Departamento de Astronomía, Universidad de Concepción, Concepción, Chile; tom@astro-udec.cl

² European Southern Observatory, Karl-Schwarzschild-Str.2, 85748 Garching, Germany

³ Instituto de Astrofísica, Pontificia Universidad Católica de Chile, Av. Vicuña Mackenna 4860, 7820436 Macul, Santiago, Chile

⁴ Institute for Astronomy, University of Hawaii, 2680 Woodlawn Drive, Honolulu, HI 96822, USA

⁵ Departamento de Ciencias Físicas, Facultad de Ciencias Exactas, Universidad Andres Bello, Fernández Concha 700, 7591538 Las Condes, Chile

⁶ Max-Planck-Institut für Astronomie, Königstuhl 17, D-69117 Heidelberg, Germany

Received / Accepted

ABSTRACT

Context. The light of the merger remnant NGC 1316 (Fornax A) is dominated by old and intermediate-age stars. The only sign of current star formation in this big galaxy is the HII region SH2, an isolated star cluster complex with a ring-like morphology and an estimated age of 0.1 Gyr at a galactocentric distance of about 35 kpc. A nearby intermediate-age globular cluster, surrounded by weak line emission and a few more young star clusters, is kinematically associated. The origin of this complex is enigmatic.

Aims. We want to investigate the nature of this star cluster complex. The nebular emission lines permit a metallicity determination which can discriminate between a dwarf galaxy or other possible precursors.

Methods. We used the Integrated Field Unit (IFU) of the VIMOS instrument at the Very Large Telescope of the European Southern Observatory in high dispersion mode to study the morphology, kinematics, and metallicity employing line maps, velocity maps, and line diagnostics of a few characteristic spectra.

Results. The line ratios of different spectra vary, indicating highly structured HII regions, but define a locus of uniform metallicity. The strong-line diagnostic diagrams and empirical calibrations point to a nearly solar or even super-solar oxygen abundance. The velocity dispersion of the gas is highest in the region offset from the bright clusters. Star formation may be active on a low level. There is evidence for a large-scale disk-like structure in the region of SH2, which would make the similar radial velocity of the nearby globular cluster easier to understand.

Conclusions. The high metallicity does not fit to a dwarf galaxy as progenitor. We favour the scenario of a free-floating gaseous complex having its origin in the merger 2 Gyr ago. Over a long period the densities increased secularly until finally the threshold for star formation was reached. SH2 illustrates how massive star clusters can form outside starbursts and without a considerable field population.

Key words. Galaxies: individual: NGC 1316 – Galaxies: kinematics and dynamics – Galaxies: star clusters

1. Introduction

NGC 1316 (Fornax A) in the outskirts of the Fornax galaxy cluster is prominent for its abundant signatures of previous galaxy interactions. Starting with the classical work of Schweizer (1980), it has been intensively studied at various wavelengths from X-rays to the radio regime (D’Onofrio et al. 1995; Shaya et al. 1996; Mackie & Fabbiano 1998; Arnaboldi et al. 1998; Longhetti et al. 1998; Kuntschner 2000; Horellou et al. 2001; Goudfrooij et al. 2001b,a; Gómez et al. 2001; Kim & Fabbiano 2003; Bedregal et al. 2006; Nowak et al. 2008; Lanz et al. 2010; Goudfrooij 2012).

Its globular cluster system has been investigated by Richtler et al. (2012a, 2014) and the planetary nebulae population by McNeil-Moylan et al. (2012). More photometric work on the cluster system has been presented by Sesto et al. (2016). Although most of the bright globular clusters show a narrow

colour range, compatible with an age of about 2 Gyr, clusters as young as 0.5 Gyr have been found in NGC 1316 (Richtler et al. 2014). However, a corresponding field stellar population of this age has not been identified until now. Even younger clusters are seen at only one place, the HII region SH2, detected by Schweizer (1980) in the southern outskirts of NGC 1316. Richtler et al. (2012b) presented the first detailed description based on HST/WFPC2 imaging in the F555W and F814W filters and VLT/FORS2 spectroscopy at 5 Å resolution.

This object is a star cluster complex containing about 100 young star clusters within a volume of radius 0.35 kpc. A peculiar feature is another nearby ensemble of blue star clusters with some line emission, grouped around an intermediate-age massive globular cluster of NGC 1316. A tentative interpretation of the nature of SH2 is that of an infalling gas-rich dwarf galaxy, as there are so many traces of previous infall processes through the rich shell system of the galaxy. We are not aware of an obvious comparable object in any other galaxy (but see the remarks on the Ruby Ring in Sect. 7.1), which does not mean that SH2 is too special to provide general insight into the process of star cluster formation. The purpose of the present contribution is to investi-

Send offprint requests to: T. Richtler

* Based on observations taken at the European Southern Observatory, Cerro Paranal, Chile, under the programme 082.B-0680, 076.B-0154, 065.N-0166, 065.N-0459.

gate in more detail the line emission, in particular the metallicity of the HII-gas, which is a key parameter for understanding the formation history of SH2 and which is expected to be low in the case of a dwarf galaxy (e.g. Smith Castelli et al. 2012).

We adopt the supernova type-Ia distance of 17.8 Mpc quoted by Stritzinger et al. (2010), corresponding to a distance modulus of $(m - M)_0 = 31.25$ mag, but see also Cantiello et al. (2013) who quote a larger distance of 20.8 Mpc. One arcsecond corresponds to 86.3 pc at a distance of 17.8 Mpc.

2. Observations and data reduction

We observed the HII region SH2 roughly centred at RA(J2000): 03h 22m 38s and Dec(J2000): $-37^\circ 18'47''$ on October 2012 in service mode with the integral-field unit (IFU) of the VISIBLE MultiObject Spectrograph (VIMOS, Le Fèvre et al. 2003) mounted on UT3 (Melipal) of the ESO Very Large Telescope in Chile. The high-resolution red (HRR) and blue (HRB) modes were used to cover the wavelength ranges 3900 – 5335 Å at $R \simeq 1700$ and 6315 – 8600 Å at $R \simeq 3100$, respectively. The field of view was chosen to be $27'' \times 27''$ with a sampling of $0.67''$ per pixel for both channels. Three individual exposures of 756 seconds were taken for each channel and accompanied by three flat-field exposures and one arc-lamp exposure. A standard star for flux calibration was also observed for each channel as part of the standard instrument calibration. The seeing during the observations was about $0.8''$.

We performed all data reduction tasks with the independent PY3D data reduction package for fibre-fed IFU spectrographs developed for the data reduction of the Calar Alto Large Integral Field Area (CALIFA) survey data (Husemann et al. 2013). It has been successfully applied to reduce VIMOS IFU data as well (e.g. Husemann et al. 2014) showing superior quality to the standard ESO pipeline. With PY3D we first process the individual exposures performing bias subtraction, cosmic ray detection with PYCOSMIC (Husemann et al. 2012), fibre tracing and extraction, wavelength calibration, fibre-to-fibre transmission correction, and flux calibration. We also homogenise the highly varying spectral resolution across the VIMOS field to be 2.5 \AA in both the HRB and HRR channel. Sky subtraction is done on each exposure by creating a high S/N mean sky spectrum from 200 fibres containing no significant object signal, which is subsequently subtracted from all fibres. Afterwards we combine the individually calibrated exposures to one datacube taking into account differential atmospheric refraction and bad pixels, such as cosmic ray hits or dead CCD pixels.

The world-coordinate system of the data is set by assigning the HST coordinates of the bright star cluster 431-1 of SH2 (Richtler et al. 2014) to the corresponding light weighted centre in the VIMOS data. For convenience we give all coordinates on the IFU in pixels, in the form X:Y for the centres of our spectral extractions (see Sect. 5.2 and Fig. 3), which can be transformed as follows into right ascension (RA) and declination (DEC), both in degrees:

$$\begin{aligned} \text{RA(J2000)} &= 50.657833 - (16 - y) \times 11.53 \times 10^{-5} \\ \text{DEC(J2000)} &= -37.313061 + (19 - x) \times 9.17 \times 10^{-5} \end{aligned}$$

3. Morphology and line maps

3.1. Appearance of the stellar cluster complex

Richtler et al. (2012a) described the appearance of SH2 on the basis of ground-based and HST imaging. The brightest cluster

(431-1) has an age of about 0.1 Gyr, based on its colour, and an estimated mass of $1.9 \times 10^5 M_\odot$, if we adopt solar metallicity. The colours indicate a mix of populations with many clusters being even younger, but the extreme crowding prohibits precise measurements. A ring-like structure of the brightest clusters is discernible. At a distance of $12''$ towards the south-west a second assembly of clusters of about the same age exists, but this time the dominant and apparently central object is an intermediate-age globular cluster of NGC 1316. Richtler et al. (2012a) estimated an age of ~ 2 Gyr and a mass of about $10^6 M_\odot$. It cannot be excluded that this is a chance projection.

3.2. Line maps

A census of line emission regarding extent and intensity in the field of SH2 is provided by Fig. 1. The upper left panel shows an HST-image, where the structure of SH2 is clearly visible (PI: A. Sandage, GO-7504). The upper right panel shows a continuum map, using the median value of the data cube of a given pixel in the HRB mode. Unfortunately, the exposure times are not sufficient to spectroscopically explore the stellar continua. Some of the very faint structure in the upper left quadrant may be flat-field residuals, but the ring of star clusters of SH2 is clearly visible. A faint population between SH2 and the globular cluster 429 is also visible towards the south-west. The colour map of Richtler et al. (2012b) indicates a somewhat redder colour than that of SH2, which is expected if a faint blue population is superimposed on a bright red galaxy background/foreground. At the same time, it is a strong argument that the cluster assembly around 429 still belongs to the SH2 complex.

The lower left panel is an $H\alpha$ map from the HRR set-up. The dynamical settings of the display make even the faintest structures visible. In particular, it shows that there is no $H\alpha$ line detected above an $S/N > 3$ between SH2 and the 429 region. The point of maximum $H\alpha$ -intensity is a rather well-defined peak and coincides more or less with the most southern point of the “ring”.

In the region of 429, there is a double structure: one peak coincides with the location of 429 itself, the other peak is shifted by about $3''$ to the north-east. A 2 Gyr old star cluster as a source of ionising radiation might appear surprising (see further details in Sect. 7.3).

The lower right panel shows the morphology of the [OIII]-5007 Å emission with the same absolute flux scaling and also clipping at a threshold of $S/N > 3$. Its morphology closely resembles that of the $H\alpha$ emission. The main part of the [OIII] emission traces the southern part of the ring, peaking roughly at the same location as $H\alpha$. The presently ionising (invisible) young stars still seem to follow the overall distribution of the 0.1 Gyr clusters.

4. Velocities and velocity maps

The knowledge of radial velocities in this region so far stems from a few sources: Schweizer (1980) quoted $\Delta v_{\text{rad}} \simeq -101$ km/s as the offset to the systemic velocity of NGC 1316, which is in excellent agreement with the HI-velocity of SH2 from Horellou et al. (2001) of 1690 km/s. Richtler et al. (2014) measured radial velocities from medium dispersion VLT/FORS2 spectra for the objects 431 and 429 from the stellar continuum and emission lines. The results are for 429: 1709 ± 12 km/s for the emission lines and 1685 ± 20 km/s for the stellar continuum, where the quoted uncertainties are internal errors of the used

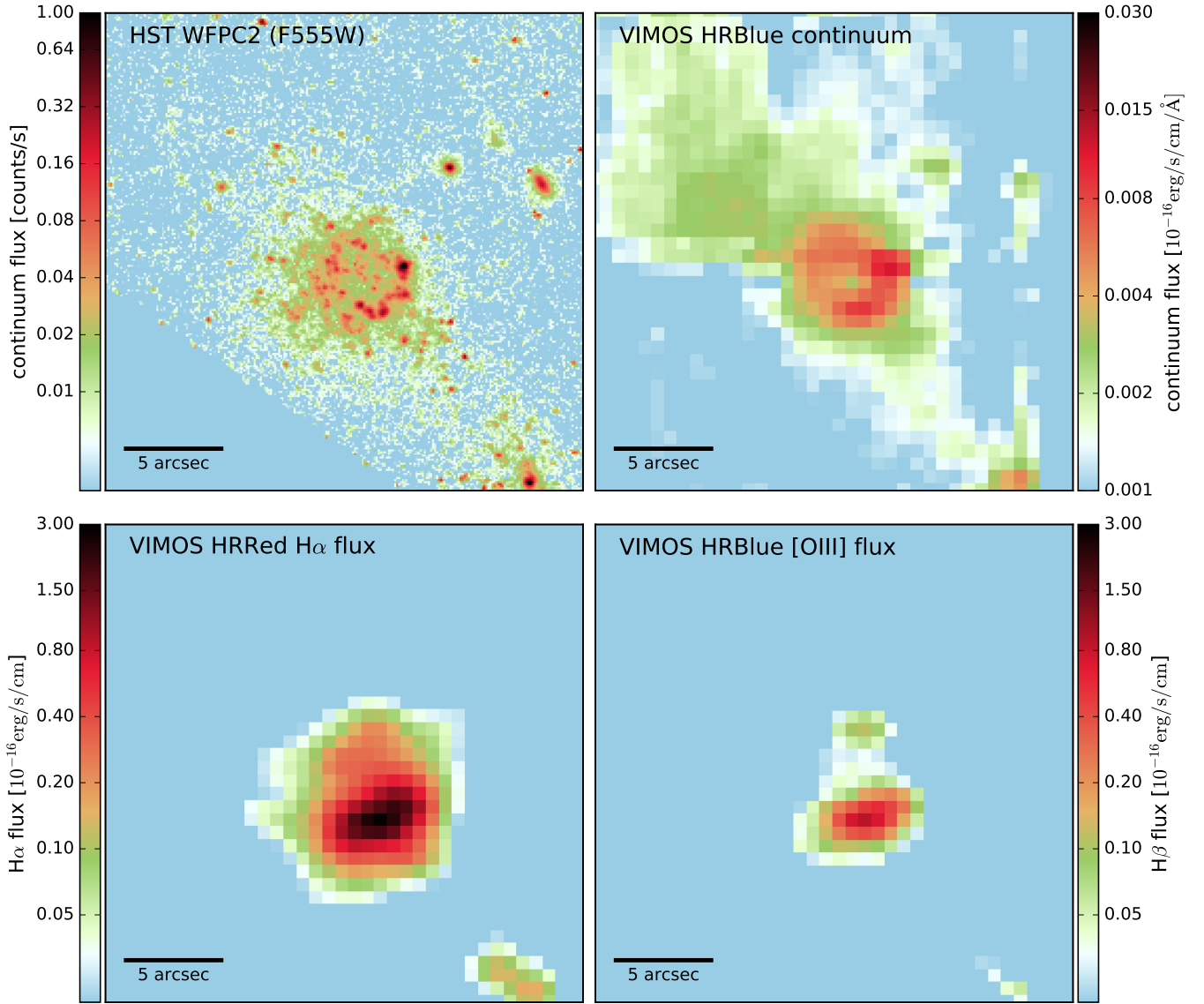


Fig. 1. HST image and line maps of SH2. All panels have a size of $27'' \times 27''$ corresponding to 2.33×2.33 kpc². The 5'' scale bar corresponds to 432 pc. (*Upper left panel*): F555W HST-WPC2 image, matching the line and continuum maps. (*Upper right panel*): Continuum map from the HRB grism spectra, using median values. (*Lower left panel*): $H\alpha$ flux map from the HRR instrument set-up. (*Lower right panel*): Map of the [OIII]-line at 5007Å using the HRB set-up. In all frames north is towards the top and east is left.

code. The velocity from emission lines for 431 is 1670 ± 20 km/s.

In Fig. 2 we show the complete kinematics maps, produced by the software *PyParadise* (Husemann et al. 2016, Husemann et al. in prep.), which is an improved version of *Paradise* (Walcher et al. 2015). The left panel of Fig. 2 displays the maps of radial velocities, the right panel displays the velocity dispersion. The pixels are not independent because of the seeing, which is slightly larger than the pixel size, but a velocity gradient or rotation is not visible. In the colour scaling of the radial velocity map, the green zone resembles approximately the interior of the ring-like arrangement of star clusters. The intermediate-age globular cluster 429 is offset by about -30 km/s with respect to the main body. While the velocity for 431 is in good agreement with that from the FORS spectra, the agreement in the case of 429 is not as good. It is, however, remarkable that 429, as a

cluster from the NGC 1316 system with a large velocity dispersion, does not show a larger velocity difference. This could be understood if the entire region were disk-like with only a small extension along the line of sight.

The velocity dispersion map shows an interesting pattern. It is low in the region of the bright clusters and distinctly higher in the northern part. This spot is also roughly coincident with the secondary maximum of the [OIII]-emission (see bottom right panel in Fig. 1). Moreover, the line ratios of this region differ from those of the cluster region. We expect a stellar projected velocity dispersion of the order of $\sigma_{LOS}^2 = \beta GM/R$, where \mathcal{M} is the mass, R a characteristic radius, and G the gravitational constant. The factor β depends on the density slope of the tracer population, the orbit anisotropy, and the mass profile. Under isotropy, $1/\sqrt{3}$ is a good guess. The dominant mass component is the HI-mass with about $10^7 M_{\odot}$ (Horellou et al. 2001),

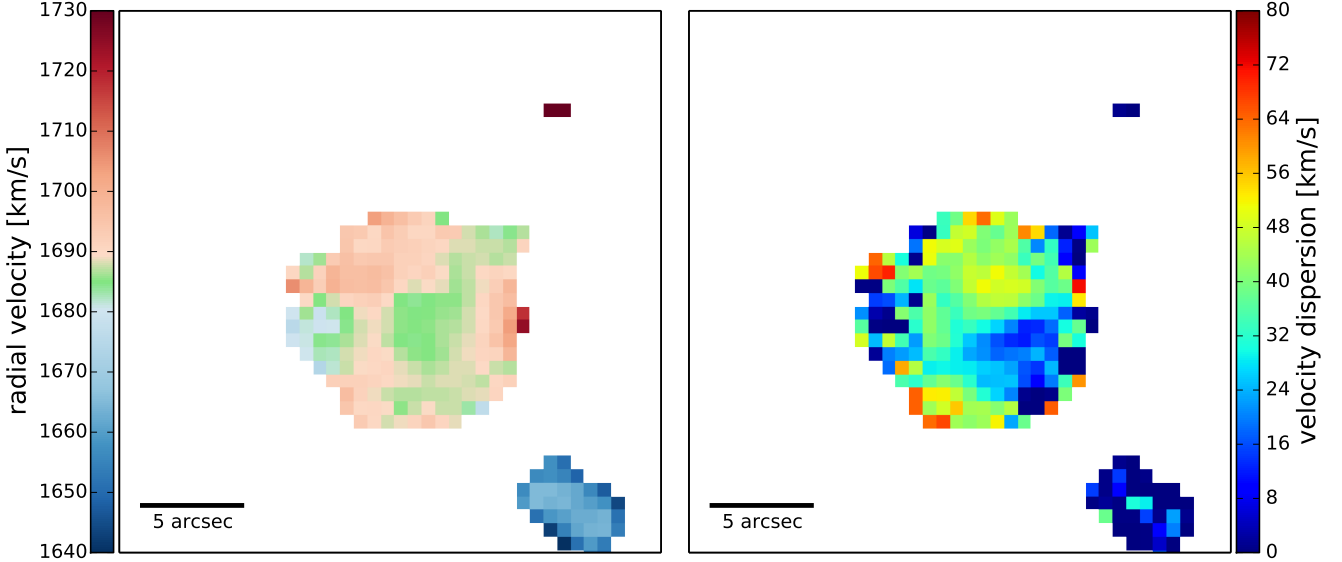


Fig. 2. (*Left panel*): Radial velocity map of the SH2 region. Neither rotation nor velocity gradients are visible. The globular cluster 429 is offset by about -30 km/s from the main body of SH2. The object in the north-western region (also visible in Fig.1) is a background galaxy without emission lines. The velocity is therefore not valid and the redshift is unknown. (*Right panel*): Velocity dispersion map of SH2. Except for the south-western region that is also the zone of the brightest $H\alpha$ -emission, the dispersion is higher than expected from simple stellar-dynamical considerations. An interesting feature is that the spot with the highest dispersion coincides with the highest [OIII]-flux intensity (see lower right panel of Fig. 1).

while the stellar mass has been estimated to be about $10^6 M_{\odot}$ (Richtler et al. 2012b). The concentration of the total mass is unknown and not resolved by VLA observations. Setting $R = 50$ pc and $\mathcal{M} = 10^7 M_{\odot}$, we expect a dispersion of about 17 km/s, which fits the southern part of the velocity map but not the high values that characterise the [OIII]-emission. Because stellar dynamics cannot produce a dispersion as high as 40 km/s, gas dynamics might be a better explanation. Shocks from supernovae and stellar winds might have left their imprints on the interstellar gas. Our data are not appropriate to investigate these possibilities in more detail. Only data with higher S/N to investigate the stellar population itself in combination with higher spectral resolution would give more insight.

5. Spectra and line fluxes

5.1. Fluxes and uncertainties

We measure the line fluxes using the IRAF command *splot*, in particular the option of fitting and subtracting the underlying stellar spectrum. The treatment of the stellar contribution (lines and continuum) is rather uncritical for the grism HRR because the blue stellar population contributes only very little flux. For example, the $H\alpha$ flux is not notably affected, while the $H\beta$ -fluxes measured in HRB are higher by about 2% if the stellar spectrum is not subtracted. Because the fainter lines are more strongly affected (by about 5%; this systematic difference disappears largely when line ratios are considered), we measured all fluxes after subtraction of the continua which have been modelled by third-degree polynomials. The fluxes and their uncertainties are given in Tables 1 and 2. The quoted uncertainties are estimated through repeated measurements and do not reflect uncertainties in the flux calibration. For [O III] and [N II], only the brighter line of the respective doublet is given. The lines [O III] 4958Å and [N II] 6548Å are always fainter by a factor of 0.34.

5.2. Extraction of some characteristic spectra

Although the substructure within SH2 is not very much larger than the seeing, there are clearly differences in the line strength ratios. To have a sample of characteristic spectra which represents the morphology and the existing line strength ratios, we chose the following (locations are given as x-y-coordinates):

1. **global**: extraction around 21:21 with a radius of 8 pixels. This sums over 197 spaxels;
2. **spot of brightest $H\alpha$ -emission**: extraction around 17:17 with a radius of 2 pixels. Average over 13 spaxels;
3. **globular cluster 429**: extraction around 4:5 with a radius of 2 pixels. Average over 13 spaxels;
4. **spot of the highest [OIII]/ $H\beta$ ratio**: extraction around 25:17 with a radius of 1 pixel. Average over 5 spaxels. This position corresponds to the planetary nebula No. 397 in the catalogue of McNeil-Moylan et al. (2012);
5. **spot of the lowest [OIII]/ $H\beta$ ratio**: extraction around 22:15 with a radius of 1 pixel. Average over 5 spaxels;
6. **star cluster 431**: extraction around 20:15 with a radius of 1 pixel. Average over 5 spaxels;
7. **north-eastern region of low $H\alpha$ -emission**: extraction around 21:20 with a radius of 2 pixels. Average over 13 spaxels.

Figure 3 shows the locations of the spectra and the approximate sizes of the extraction radii. Figure A.1 displays the total spectrum. We do not show the others because of their similar appearance.

5.3. $H\alpha$ -flux and star formation rate

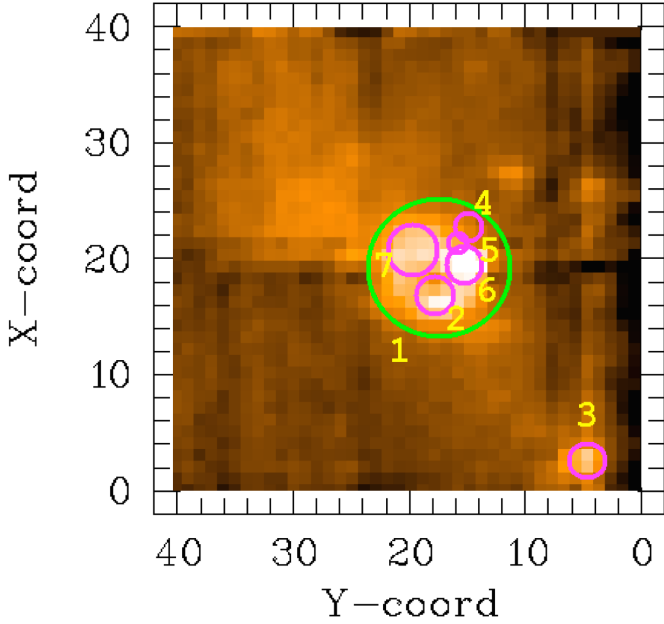
We measure the $H\alpha$ -flux in spectrum 1 that averages over a radius of 8 pixels (see Section 5.2). The flux is 60.5×10^{-16} erg/s/cm² and the luminosity 2.17×10^{38} erg/s. Adopting for

Table 1. Line fluxes in several selected spectra obtained with HRB. The fluxes are in units of 10^{16} erg/s/cm².

ID	spectrum	H δ	H γ	H β	[O III]
wavelength		4101	4340	4861	5007
1	21:21 (sum)	2.44 \pm 0.04	6.21 \pm 0.1	16.50 \pm 0.2	11.63 \pm 0.2
2	17:17 (average)	0.10 \pm 0.005	0.21 \pm 0.005	0.52 \pm 0.01	0.46 \pm 0.008
3	4:5 (average)	?	?	0.037 \pm 0.002	0.026 \pm 0.001
4	25:17 (average)	0.012 \pm 0.002	0.017 \pm 0.002	0.039 \pm 0.002	0.058 \pm 0.003
5	22:15 (average)	0.013 \pm 0.002	0.025 \pm 0.001	0.074 \pm 0.003	0.026 \pm 0.002
6	20:15 (average)	0.03 \pm 0.002	0.065 \pm 0.002	0.20 \pm 0.003	0.088 \pm 0.002
7	21:20 (average)	0.01 \pm 0.002	0.03 \pm 0.002	0.077 \pm 0.003	0.027 \pm 0.002

Table 2. Line fluxes in several selected spectra obtained with HRR. The fluxes are in units of 10^{16} erg/s/cm².

ID	spectrum	H α	[N II]	He I	[S II]	[S II]	[Ar III]
wavelength		6563	6582	6678	6715	6731	7135
1	21:21 (sum)	60.23 \pm 0.3	21.18 \pm 0.2	0.52 \pm 0.03	8.77 \pm 0.1	6.03 \pm 0.1	1.16 \pm 0.05
2	17:17 (average)	2.05 \pm 0.02	0.71 \pm 0.02	0.02 \pm 0.002	0.22 \pm 0.01	0.16 \pm 0.01	0.05 \pm 0.002
3	4:5 (average)	0.082 \pm 0.004	0.028 \pm 0.002	...	0.006 \pm 0.001	0.007 \pm 0.001	0.002 \pm 0.0003
4	25:17 (average)	0.087 \pm 0.002	0.033 \pm 0.002	...	0.02 \pm 0.001	0.012 \pm 0.001	...
5	22:15 (average)	0.14 \pm 0.002	0.052 \pm 0.002	0.005 \pm 0.0005	0.03 \pm 0.001	0.02 \pm 0.001	0.001 \pm 0.0002
6	20:15 (average)	0.61 \pm 0.01	0.21 \pm 0.003	...	0.08 \pm 0.002	0.06 \pm 0.002	0.01 \pm 0.001
7	21:20 (average)	0.23 \pm 0.01	0.08 \pm 0.003	...	0.048 \pm 0.002	0.03 \pm 0.002	...


Fig. 3. The approximate locations and approximate sizes of the extraction radii of our characteristic spectra. The image is the median of the HRblue data cube. The unusual X-Y-configuration reflects the axes on the original data cube.

the star formation rate the conversion of Panuzzo et al. (2003), $\text{SFR}/\text{H}\alpha\text{-luminosity} = 7.05 \times 10^{-49} M_{\odot}/\text{erg}$, the SFR is $2.2 \cdot 10^{-4} M_{\odot}/\text{yr}$ or $3 \cdot 10^{-4} M_{\odot}/\text{yr}/\text{kpc}^2$, much lower than a starburst, and still lower than “normal” star formation rates in normal galaxies (Wuyts et al. 2011). Clearly, there must have been a starburst 0.1 Gyr ago with a much higher H α -flux of which we now only see the aftermath.

6. Diagnostic graphs

6.1. Models from Dopita et al. (2013)

The precise determination of element abundances in HII regions normally relies on the determination of electron temperatures, where [OIII]-4636Å is the most important line. However, this line is not visible in any of our spectra, which indicates a low temperature and therefore a high metallicity with enhanced cooling capability. This also fits the fact that neutral He-lines are visible. Consequently, we use strong-line diagnostic diagrams to estimate the oxygen abundance of SH2. There is a huge amount of literature on HII regions and how to use strong-line diagnostic diagrams. We refer to Dopita et al. (2013) and Nicholls et al. (2014) as the primary links with the history of HII region diagnostics. These authors revisit the physics of HII regions, using the most recent atomic line parameters, with the motivation that the energy distribution of electrons might be a κ -distribution rather than Boltzmann-Maxwellian ($\kappa = \infty$). These works present many diagnostic diagrams using strong lines, of which only a few are useful for us due to the restricted wavelength range. Furthermore, reliable line-ratios are preferably constructed from lines from either HRB or HRR. This leaves us with the diagnostic line ratios [OIII]/H β , [NII]/H α , [SII]/H α , and [NII]/[SII], which correspond to the diagrams Fig. 9, Fig. 10, and Fig. 22 of Dopita et al. (2013) (in the case of [NII], we refer to the 6548Å line, in the case of [SII] to the sum of the 6715Å and 6731Å lines). The [ArIII]-line at 7135Å is too weak to permit sensible measurements. The line ratios and the locations of our selected spectra in these diagnostic diagrams are shown in Table 3 and in Fig. 4. Their uncertainties are calculated by error propagations of the uncertainties shown in Tables 1 and 2.

The models are taken from Dopita et al. (2013) and use the ionisation parameter $\log q$ and the oxygen abundance as parameters. The abundances in solar units are indicated in all panels by the numbers 0.5, 1, 2, 3. The interval of $\log q$ values, which is the same for all models, is indicated as well. According to the definition of Dopita et al. (2013), q is the number of ionising photons passing through a unit area divided by the number density of neutral atoms and ions. High q -values are therefore

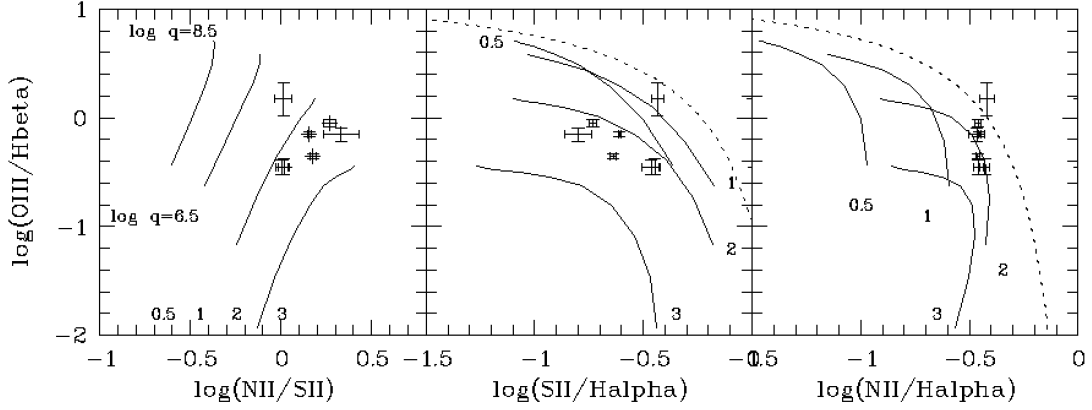


Fig. 4. Diagnostic graphs for six selected emission line spectra in SH2 (see Table 3 and Section 5.2 for explanation). These spectra are compared to HII region models from Dopita et al. (2013) with the ionisation parameter $\log q$ and four oxygen abundances ($0.5 \times$ solar, solar, $2 \times$ solar, and $3 \times$ solar) as parameters. The solid lines are lines of constant oxygen abundance and varying $\log q$. In the left panel, the range of $\log q$ values is indicated, and is the same for all panels. The models refer to $\kappa = \infty$ (corresponding to a Boltzmann electron distribution). The dotted lines in the middle and right panels separate HII regions from AGN- and LINER-spectra according to Kewley et al. (2001). All spectra except 25:17 are consistent with a uniform abundance value, although $[\text{OIII}]/\text{H}\beta$ varies significantly. The middle and the right graph show the degeneracy for high metallicities that is not present in the left graph. A super-solar oxygen abundance is supported by all three diagnostic graphs.

Table 3. Diagnostic line ratios (Cols. 3 - 7) and results from empirical calibrations (Cols. 8 - 10). See Sect. 5.2 for the properties of the spectra. The ID numbers are identified in Fig. 4.

ID	spectrum	$\log [\text{OIII}]/\text{H}\beta$	$\log [\text{NII}/\text{SII}]$	$\log [\text{SII}]/\text{H}\alpha$	$\log [\text{NII}]/\text{H}\alpha$ (N2)	O3N2	Z(N2)	Z(O3N2)	Z(PG)
1	21:21	-0.15 ± 0.03	0.16 ± 0.03	-0.61 ± 0.01	-0.45 ± 0.01	0.30 ± 0.03	8.53 ± 0.03	8.46 ± 0.01	8.57
2	17:17	-0.05 ± 0.03	0.27 ± 0.11	-0.73 ± 0.03	-0.46 ± 0.02	0.41 ± 0.04	8.53 ± 0.03	8.44 ± 0.03	8.58
3	4:5	-0.15 ± 0.06	0.33 ± 0.31	-0.80 ± 0.14	-0.47 ± 0.08	0.31 ± 0.10	8.53 ± 0.03	8.47 ± 0.03	8.60
4	25:17	0.17 ± 0.15	0.01 ± 0.13	-0.43 ± 0.04	-0.42 ± 0.05	0.59 ± 0.16	8.55 ± 0.03	8.41 ± 0.03	8.56
5	22:15	-0.45 ± 0.07	0.02 ± 0.08	-0.45 ± 0.03	-0.43 ± 0.03	-0.02 ± 0.08	8.54 ± 0.03	8.53 ± 0.03	8.53
6	20:15	-0.36 ± 0.02	0.18 ± 0.04	-0.64 ± 0.03	-0.46 ± 0.02	0.11 ± 0.03	8.53 ± 0.03	8.51 ± 0.03	8.56
7	21:20	-0.46 ± 0.03	0.18 ± 0.04	-0.64 ± 0.03	-0.46 ± 0.02	0.11 ± 0.03	8.53 ± 0.03	8.53 ± 0.03	8.60

realised when the ionising sources are nearby (planetary nebulae) and/or when the spectrum of ionising photons is harder than that produced by an OB stellar population. Another effect is that for high metallicities, some indices are folded back onto the regime of lower metallicities because the enhanced cooling diminishes the fraction of ionised species with respect to hydrogen. Therefore, there is a limit that line ratios of HII regions normally do not cross and which can be used to distinguish the line ratios of HII regions from those of AGNs and LINERs. These limits (which in reality are not very strict) are taken from Kewley et al. (2001), and are indicated for the middle and the right panel by the dotted lines. The $\log q$ and abundances are best separated in the left panel, where the lines of constant $\log q$ are almost vertical. It is satisfactory that although $\log q$ varies, the loci of the spectrum follow a constant abundance line with the exception of 25-17. This is also the case in the middle panel, although there is the above-mentioned degeneracy, in the sense that metal-rich loci cross with the metal-poor ones. The right panel indicates a somewhat lower abundance.

For the interpolation in the tables of Dopita et al. (2013), we use linear expressions in the intervals of interest, which are $\log q > 7.0$ and $1 < z \leq 3$. For the left panel, we obtain (valid only for

this selection)

$$z = 1.8(\pm 0.06) + 1.8(\pm 0.1) \times \log[\text{NII}/\text{SII}] - 1.1(\pm 0.03) \times \log[\text{OIII}] \quad (1)$$

For the middle panel, we obtain

$$z = 1.44(\pm 0.06) - 1.42(\pm 0.1) \times \log[\text{SII}/\text{H}\alpha] - 1.4(\pm 0.08) \times \log[\text{OIII}] \quad (2)$$

For the right panel, we adopt the value $z=2.0$ with the exception of spectrum 4.

Neglecting spectrum 4, the resulting oxygen abundances (in solar units) are 2.44 ± 0.15 for the left panel and 2.31 ± 0.2 for the middle panel. With the the solar abundance $12 + \log(\text{O}/\text{H})=8.69$ (Grevesse et al. 2010), these values transform to $12 + \log(\text{O}/\text{H})=9.08$ and 9.05 , respectively. The right panel gives $12 + \log(\text{O}/\text{H})=8.99$.

A comparison with the parameters of the HII regions of van Zee et al. (1998), provided by Dopita et al. in their graphs, shows that SH2 belongs to the HII regions with the highest abundance and highest ionisation parameters known. Spectrum 4, the spectrum with the highest ionisation parameter, deviates in that the abundance is not consistent with the other spectra. As mentioned before, the position is consistent with PN 397 in the catalogue of McNeil-Moylan et al. (2012). The velocity from this catalogue

is 1731 ± 30 km/s, also consistent with an affiliation to SH2. However, there are more PNe in this region with similar velocities that certainly do not belong to SH2. Moreover, the $[\text{OIII}]/\text{H}\beta$ ratio is quite small compared with other planetary nebulae. We cannot decide whether this is a true planetary nebula or a particularly high ionisation flux in the HII region, and we leave it as an interesting case.

6.2. Empirical calibrations of oxygen abundance

To date there is no commonly accepted metallicity scale for HII regions. Abundances that have been obtained via determinations of electron temperatures are often lower by 0.3 - 0.5 dex than those that have been obtained via photoionisation models (e.g. Bresolin et al. 2009; see also the discussion section in Pilyugin & Grebel 2016). The reasons are still under debate. Indeed, we also see this discrepancy in our data when we apply empirical calibrations.

6.2.1. Calibration by Marino et al. 2013

Marino et al. (2013) use the CALIFA data set and temperature-based abundances in the literature, to update the calibrations for the indicators N2 and O3N2, being

$$\begin{aligned} \text{N2} &= \log([\text{NII}]6584/\text{H}\alpha) \text{ and} \\ \text{O3N2} &= \log\left\{\frac{([\text{OIII}]5007/\text{H}\beta)}{([\text{NII}]6584/\text{H}\alpha)}\right\}. \end{aligned}$$

In these calibrations, HII regions appear with the abundance as the only parameter, which in the case of high metallicity is degenerated. The proposed calibrations are

$$12 + \log(\text{O}/\text{H}) = 8.533 - 0.214 \times \text{O3N2} \quad (3)$$

and

$$12 + \log(\text{O}/\text{H}) = 8.743 + 0.462 \times \text{N2} \quad (4)$$

The values of these parameters for our spectra are listed in Cols. 6 - 9 in Table 3. The calibrations result in mean oxygen abundances of $12 + \log[\text{O}/\text{H}] = 8.53 \pm 0.009$ for N2 and $12 + \log[\text{O}/\text{H}] = 8.48 \pm 0.05$ for O3N2, where the uncertainties have been calculated by error propagation using the uncertainties in the calibrating relations. As expected, these values are systematically lower, by approximately 0.5 dex, than those obtained in Sect. 6.1 from photoionisation models. For the following discussion, however, it is worth pointing out that even the empirical calibrations indicate an oxygen abundance corresponding to about 60% solar.

6.2.2. Calibration of Pilyugin & Grebel 2016

An empirical calibration with a small scatter of 0.1 dex has been presented by Pilyugin & Grebel (2016), who use temperature-based abundances of HII regions to construct relations between three strong-line indices and abundances. They calibrate the following indices in terms of oxygen abundance: $\text{N2} = (6548 + 6583)/\text{H}\beta$, $\text{S2} = (6715 + 6731)/\text{H}\beta$, $\text{R3} = (4958 + 5007)/\text{H}\beta$, where the wavelengths stand for the fluxes of the respective lines (they calibrate additional indices involving $[\text{OII}] 3727\text{\AA}$ that are not relevant for us). Only for R3 can we measure all fluxes using the same spectrum, and so we adopt $\text{H}\alpha = 2.89 \times \text{H}\beta$ for N2 and S2. We use equation (6) of Pilyugin & Grebel (2016) to derive for our spectra a mean oxygen abundance of $12 + \log[\text{O}/\text{H}] = 8.55 \pm 0.05$, where the uncertainty is the standard deviation.

The abundances from the calibrations using T_e -based methods are thus in very good mutual agreement, but distinctly lower than the values from the diagnostic graphs. However, irrespective of the absolute value, an abundance of $12 + \log[\text{O}/\text{H}] = 8.55$ still belongs to the most metal-rich HII regions in the calibrating sample of Pilyugin & Grebel (2016) where the extreme value is 8.7.

7. Discussion

7.1. Possible formation and evolution of SH2

The high oxygen abundance of SH2 which is indicated by both the line diagnostics and empirical calibrations, excludes the nature of SH2 as a dwarf galaxy. According to the mass-metallicity relation for dwarf galaxies, an oxygen abundance of $12 + \log(\text{O}/\text{H}) = 7.74$ (solar abundance $12 + \log(\text{O}/\text{H}) = 8.69$) is expected for a stellar mass of $10^6 M_\odot$, or $12 + \log(\text{O}/\text{H}) = 7.85$ if the total HI mass of $10^7 M_\odot$ is inserted (e.g. Izotov et al. 2015), aside from the fact that such an extremely gas-rich dwarf galaxy would be quite exotic, in particular in close vicinity to a giant galaxy such as NGC 1316. This high abundance of SH2 rather fits to solar metallicities that have been determined for some bright globular clusters in NGC 1316 (Goudfrooij et al. 2001b). These clusters were probably formed during a period of very high star formation ~ 2 Gyr ago which generated a major part of the field stellar population (Richtler et al. 2012a). However, globular cluster formation did not cease after the main starburst. We found one globular cluster (there are perhaps more) with an age of about 0.5 Gyr (the object n1316-gc01178 of Richtler et al. 2012a) without an obvious field component of this age (Richtler et al. 2014). The complex SH2, after being dispersed, will provide the globular cluster system of NGC 1316 with more young star clusters without contributing much to the field stellar population.

Since there is no evidence for recent star formation in NGC 1316 and no direct evidence for the existence of larger molecular cloud complexes outside the central regions (Lanz et al. 2010), the parent cloud of SH2 must have been quite isolated, but was not unique in NGC 1316. A few arcminutes to the north, Mackie & Fabbiano (1998) found an “extended emission line region (EELR)”. The ionising photons seemingly do not come from a young stellar population as in the case of SH2. The HI mass is about $10^7 M_\odot$, similar to SH2. The colour map shown by Richtler et al. (2012b) reveals a reddish patch, indicative of dust. The basic difference between SH2 and the EELR seems to be the occurrence of star formation. It can be that the EELR is in an earlier evolutionary stage than SH2 and a starburst is still to come.

The question is whether it needs an external trigger like ram pressure or a tidal shock to commence star formation. We find a similar situation in many blue compact dwarfs, which show recent clustered star formation even in very isolated locations after a long period of quiescence (Fuse et al. 2012). We also mention the possibility of “jet-induced star formation” that has been discussed, for example to explain the existence of a young stellar population near Centaurus A at a galactocentric distance of 15 kpc (Mould et al. 2000; Santoro et al. 2016; Salomé et al. 2016). In that case the age of SH2 would indicate the epoch of the last nuclear activity in NGC1316. The fact that the radio jet in NGC1316 and the line nucleus-SH2 are strongly misaligned is perhaps no counterargument because of the differential rotation and precession of the jet. However, there is no further evidence for this interesting process.

A possible scenario is that of a slow long-term evolution of molecular material where the critical density for star formation evolves over a time span of several Gyrs. That a molecular cloud complex survives without star formation much longer than about 10^8 years is not easily understandable, so it is more probable that molecules formed inside the densest parts of an original HI complex during a long period of 1 – 2 Gyr. Once a molecular cloud core has formed and is shielded, there is hardly anything that can prevent star formation from beginning (e.g. Elmegreen 2007) and many bound star clusters can form in high-density peaks (see e.g. Kruijssen 2012).

To understand the nature of SH2, it would be helpful to compare it with other objects. But regarding the combination of the principal characteristics such as extreme clustering, ring-like morphology, and isolation, SH2 seems to be unique in the literature. This would not be surprising, if this kind of star formation were exclusively found in the aftermath of mergers. To our knowledge, even nearby prominent mergers like NGC 474 are not surveyed to this detail. However, considering these properties separately, extreme clustering is also found in the starbursts of dwarf galaxies (Adamo et al. 2011), for example in Haro 11 (Adamo et al. 2010) where even more clusters than in SH2 are crowded together within a similar volume. A ring-like cluster configuration, known as the Ruby Ring, has been identified in NGC 2146 (Adamo et al. 2012). The authors offer an explanation based on the existence of a central massive star cluster where supernovae and stellar winds sweep up the interstellar medium to trigger secondary star formation in a ring. In the case of SH2, an obvious central object is missing, but one may speculate that 10^8 years ago, the brightest object 431, now displaced, was the central cluster. In that case, one would expect the “ring population” to be considerably younger, which at least for the ionising population apparently is the case.

7.2. A failed UCD?

Intermediate-age star clusters are found in NGC1316 with masses as high as about $2 \times 10^7 M_{\odot}$ (Goudfrooij et al. 2001b; Richtler et al. 2014) that accordingly can be labeled Ultracompact Dwarfs (UCDs) (e.g. Hilker et al. 2007). The global star formation efficiency in SH2 is quite low considering the total gas mass of about $10^7 M_{\odot}$. We do not know why a more massive object has not formed, but we can estimate that the present configuration is unlikely to merge and form one object. The ring-like appearance strongly indicates a gas disk at the time of formation. If we assume as an extreme that the total mass is inside the ring, we expect a rotation velocity of about 10 km/s, probably lower than the velocity dispersion within this zone of NGC1316. We therefore expect it to be a transient configuration that will disperse.

7.3. Role of the star cluster complex 429

The intermediate-age massive globular cluster 429 is not easily brought into connection with SH2. If the three-dimensional structure in the region, including globular clusters, was more or less isotropic, the agreement of the radial velocities of this object and SH2, including all line emission, would be a very surprising coincidence. If, on the other hand, we consider a large-scale disk, the difficulty of explaining the connection of 429 with SH2 disappears. In this case, 429 would only be a cluster casually orbiting nearby. A hint might be the peak in the distribution of globular cluster velocities at about 1600 km/s, which is in quite

good agreement with the velocity of 429 (Richtler et al. 2012b) and may be interpreted as a disk population. A stronger constraint can come from the kinematics of the galaxy light itself, because a disk should be recognisable by its low velocity dispersion. However, our signal-to-noise ratio is too low for this kind of analysis.

Another interesting feature is that this 2 Gyr old cluster is apparently capable of ionising its environment which may seem surprising at first. However, post-AGB stars of much older populations ionise gas in early-type galaxies (Stasińska et al. 2008; Cid Fernandes et al. 2011; Kehrig et al. 2012; Johansson et al. 2014). According to Fig. 2 of Cid Fernandes et al. (2011), the flux of HI-ionising photons increases by two orders of magnitudes at an age of about 0.1 Gyr and then remains at an almost constant level. We are not aware of any other example in the literature that indicates an ionising photons flux from an intermediate-age globular cluster.

8. Summary and conclusions

We have investigated the emission lines of the isolated HII region and star cluster complex SH2 in the merger remnant NGC 1316 with data from the VIMOS/IFU at the Very Large Telescope. Our objective was to test the hypothesis of SH2 being an infalling dwarf galaxy. We used strong-line diagnostic diagrams and empirical calibrations to determine the metallicity of the gas and arrive at a nearly solar or even super-solar oxygen abundance. The high metallicity of SH2 disfavors the interpretation of an infalling dwarf galaxy and favours a scenario where a molecular cloud complex, perhaps formed during the merger ~ 2 Gyr ago, was quiescent for a long time and started to form stars about 0.1 Gyr ago. Its isolated character might come from a dynamically chaotic situation during a merger/infall event when large coherent structures (perhaps molecular in nature) were disrupted and started their own dynamical life. A long-term evolution of the molecular material then resulted finally in a critical density for star formation perhaps without an external triggering event. This also explains the existence of a few massive star clusters in NGC 1316 with ages of about 0.5 Gyr without a significant field component.

The association with the intermediate-age cluster 429 remains unclear. The concordant radial velocities might reflect a disk-like kinematic seen face-on. The dense clustering is also found in star-forming dwarf galaxies, and even the ring-like morphology finds its analogue in NGC 2146. SH2 is an illustrative example of massive star cluster formation outside of starburst periods.

Acknowledgements. We thank the referee, Søren S. Larsen, for a constructive report and helpful suggestions that improved the paper. T.R. acknowledges support from the BASAL Centro de Astrofísica y Tecnologías Afines (CATA) PFB-06/2007. T.R. thanks ESO/Garching for a science visitorship that was essential for the present work. T.H.P. acknowledges support by a FONDECYT Regular Project Grant (No. 1161817) and the BASAL Center for Astrophysics and Associated Technologies (PFB-06).

Appendix A: Spectra

References

- Adamo, A., Östlin, G., & Zackrisson, E. 2011, MNRAS, 417, 1904
- Adamo, A., Östlin, G., Zackrisson, E., et al. 2010, MNRAS, 407, 870
- Adamo, A., Smith, L. J., Gallagher, J. S., et al. 2012, MNRAS, 426, 1185
- Arnaboldi, M., Freeman, K. C., Gerhard, O., et al. 1998, ApJ, 507, 759
- Bedregal, A. G., Aragón-Salamanca, A., Merrifield, M. R., & Milvang-Jensen, B. 2006, MNRAS, 371, 1912

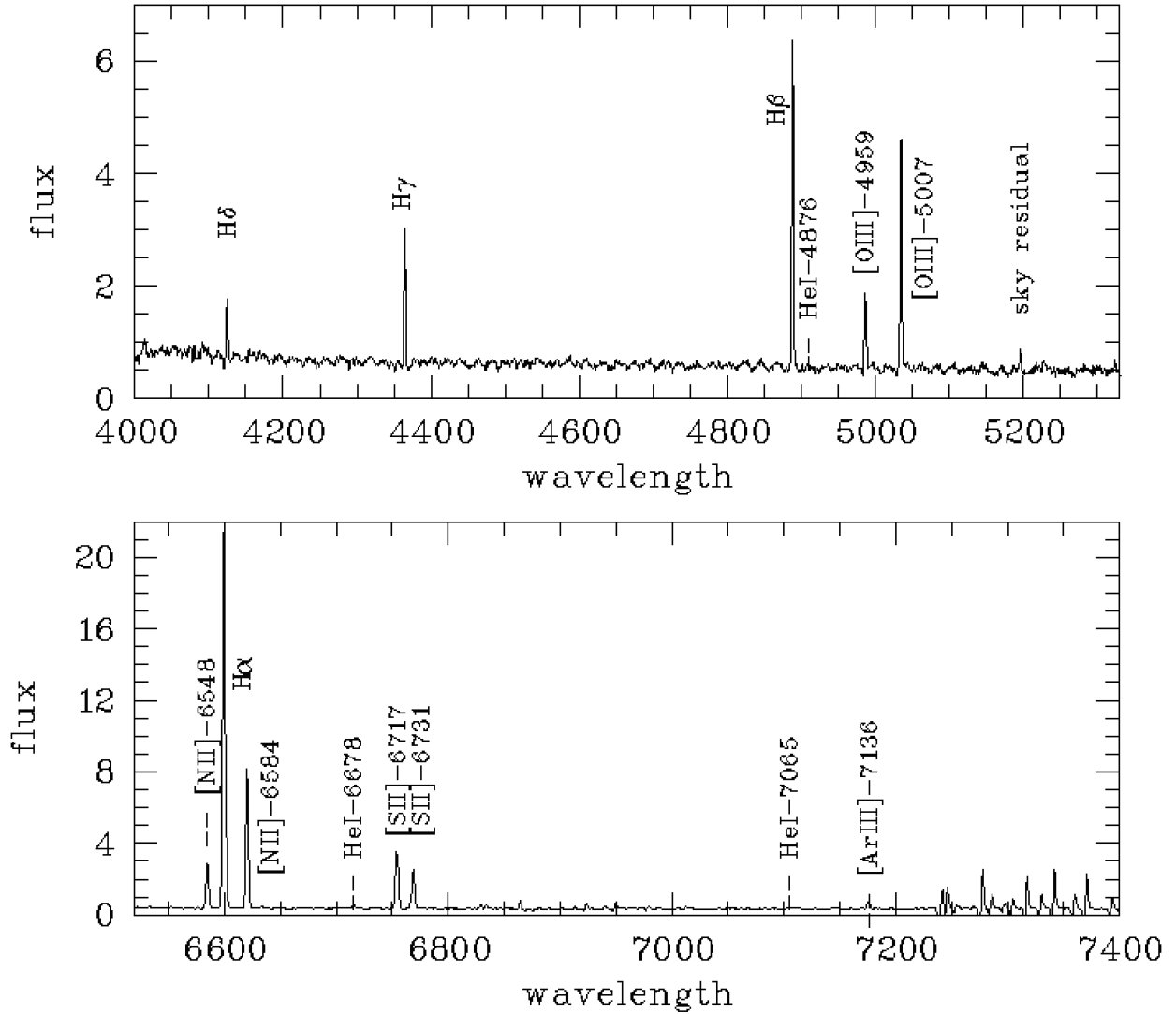


Fig. A.1. Total spectrum. The flux is the sum of an extraction centred on 21:21 and summed up within a radius of eight pixels. The upper panel shows the spectrum from the grism HRB, the lower from the grism HRR. The visibility of HeI lines and the absence of the OII-4636 line already indicate a low temperature and accordingly a high metallicity, which is confirmed by a more detailed line diagnostics.

- Bresolin, F., Gieren, W., Kudritzki, R.-P., et al. 2009, *ApJ*, 700, 309
Cantiello, M., Grado, A., Blakeslee, J. P., et al. 2013, *A&A*, 552, A106
Cid Fernandes, R., Stasińska, G., Mateus, A., & Vale Asari, N. 2011, *MNRAS*, 413, 1687
D’Onofrio, M., Zaggia, S. R., Longo, G., Caon, N., & Capaccioli, M. 1995, *A&A*, 296, 319
Dopita, M. A., Sutherland, R. S., Nicholls, D. C., Kewley, L. J., & Vogt, F. P. A. 2013, *ApJS*, 208, 10
Elmegreen, B. G. 2007, *ApJ*, 668, 1064
Fuse, C., Marcum, P., & Fanelli, M. 2012, *AJ*, 144, 57
Gómez, M., Richtler, T., Infante, L., & Drenkhahn, G. 2001, *A&A*, 371, 875
Goudfrooij, P. 2012, *ApJ*, 750, 140
Goudfrooij, P., Alonso, M. V., Maraston, C., & Minniti, D. 2001a, *MNRAS*, 328, 237
Goudfrooij, P., Mack, J., Kissler-Patig, M., Meylan, G., & Minniti, D. 2001b, *MNRAS*, 322, 643
Grevesse, N., Asplund, M., Sauval, A. J., & Scott, P. 2010, *Ap&SS*, 328, 179
Hilker, M., Baumgardt, H., Infante, L., et al. 2007, *A&A*, 463, 119
Horellou, C., Black, J. H., van Gorkom, J. H., et al. 2001, *A&A*, 376, 837
Husemann, B., Bennert, V. N., Scharwächter, J., Woo, J.-H., & Choudhury, O. S. 2016, *MNRAS*, 455, 1905
Husemann, B., Jahnke, K., Sánchez, S. F., et al. 2013, *A&A*, 549, A87
Husemann, B., Jahnke, K., Sánchez, S. F., et al. 2014, *MNRAS*, 443, 755
Husemann, B., Kamann, S., Sandin, C., et al. 2012, *A&A*, 545, A137
Izotov, Y. I., Guseva, N. G., Fricke, K. J., & Henkel, C. 2015, *MNRAS*, 451, 2251
Johansson, J., Woods, T. E., Gilfanov, M., et al. 2014, *MNRAS*, 442, 1079
Kehrig, C., Monreal-Ibero, A., Papaderos, P., et al. 2012, *A&A*, 540, A11
Kewley, L. J., Dopita, M. A., Sutherland, R. S., Heisler, C. A., & Trevena, J. 2001, *ApJ*, 556, 121
Kim, D.-W. & Fabbiano, G. 2003, *ApJ*, 586, 826
Kruijssen, J. M. D. 2012, *MNRAS*, 426, 3008
Kuntschner, H. 2000, *MNRAS*, 315, 184
Lanz, L., Jones, C., Forman, W. R., et al. 2010, *ApJ*, 721, 1702
Le Fèvre, O., Saisse, M., Mancini, D., et al. 2003, in *Proc. SPIE*, Vol. 4841, *Instrument Design and Performance for Optical/Infrared Ground-based Telescopes*, ed. M. Iye & A. F. M. Moorwood, 1670–1681
Longhetti, M., Rampazzo, R., Bressan, A., & Chiosi, C. 1998, *A&AS*, 130, 267
Mackie, G. & Fabbiano, G. 1998, *AJ*, 115, 514
Marino, R. A., Rosales-Ortega, F. F., Sánchez, S. F., et al. 2013, *A&A*, 559, A114
McNeil-Moylan, E. K., Freeman, K. C., Arnaboldi, M., & Gerhard, O. E. 2012, *ArXiv e-prints*
Mould, J. R., Ridgeway, A., Gallagher, III, J. S., et al. 2000, *ApJ*, 536, 266
Nicholls, D. C., Dopita, M. A., Sutherland, R. S., et al. 2014, *ApJ*, 786, 155
Nowak, N., Saglia, R. P., Thomas, J., et al. 2008, *MNRAS*, 391, 1629
Panuzzo, P., Bressan, A., Granato, G. L., Silva, L., & Danese, L. 2003, *A&A*,

409, 99

- Pilyugin, L. S. & Grebel, E. K. 2016, *MNRAS*, 457, 3678
- Richtler, T., Bassino, L. P., Dirsch, B., & Kumar, B. 2012a, *A&A*, accepted, Paper I
- Richtler, T., Hilker, M., Kumar, B., et al. 2014, *A&A*, 569, A41
- Richtler, T., Kumar, B., Bassino, L. P., Dirsch, B., & Romanowsky, A. J. 2012b, *A&A*, 543, L7
- Salomé, Q., Salomé, P., Combes, F., Hamer, S., & Heywood, I. 2016, *A&A*, 586, A45
- Santoro, F., Oonk, J. B. R., Morganti, R., Oosterloo, T. A., & Tadhunter, C. 2016, *A&A*, 590, A37
- Schweizer, F. 1980, *ApJ*, 237, 303
- Sesto, L. A., Faifer, F. R., & Forte, J. C. 2016, *MNRAS*, 461, 4260
- Shaya, E. J., Dowling, D. M., Currie, D. G., et al. 1996, *AJ*, 111, 2212
- Smith Castelli, A. V., Cellone, S. A., Faifer, F. R., et al. 2012, *MNRAS*, 419, 2472
- Stasińska, G., Vale Asari, N., Cid Fernandes, R., et al. 2008, *MNRAS*, 391, L29
- Stritzinger, M., Burns, C. R., Phillips, M. M., et al. 2010, *AJ*, 140, 2036
- van Zee, L., Salzer, J. J., Haynes, M. P., O'Donoghue, A. A., & Balonek, T. J. 1998, *AJ*, 116, 2805
- Walcher, C. J., Coelho, P. R. T., Gallazzi, A., et al. 2015, *A&A*, 582, A46
- Wuyts, S., Förster Schreiber, N. M., van der Wel, A., et al. 2011, *ApJ*, 742, 96